La mer 63 : 95–121, 2025, https://doi.org/10.32211/lamer.63.3-4_95
Société franco-japonaise d'Océanographie, Tokyo

Spatiotemporal variability and ENSO modulation of subsurface anticyclonic eddies (Puddies) in the Peru-Chile eastern boundary upwelling system

Gandy Maria ROSALES QUINTANA[1)], Takeyoshi NAGAI[2)], and Luis Alfredo ICOCHEA SALAS[3)]

Abstract: In eastern boundary upwelling systems (EBUSs), eddies are crucial for offshore transport of biogeochemical tracers and their vertical exchanges. We investigate the spatial and temporal variability of subsurface-intensified anticyclonic eddies (Puddies) in the Peruvian EBUS using high-resolution reanalysis and observations. Results show that subsurface intensified anticyclonic eddies dominate the subsurface layer, accounting for 54% of the total number of subsurface eddies. They exhibit a marked seasonal cycle, peaking in austral autumn closely aligned with eddy kinetic energy and Peru-Chile Undercurrent (PCUC) variability. The number of subsurface intensified anticyclonic eddies increases during El Niño events (1997–1998, 2015–2016), and moderately warm years (2008, 2012 and 2014), coinciding with a deepening of the $\sigma_\theta = 26$–isopycnal near the coast, as the equatorial warm pool propagates poleward as the coastal trapped waves. This propagating deepening of the isopycnal intensifies the PCUC and fosters greater subsurface eddy generation. Several methods were used to estimate the phase speed of the propagation. For the reanalysis data, the poleward phase speeds of the first baroclinic mode internal Kelvin wave obtained by solving the vertical modal equation range from 0.8 to 1.7 m s^{-1} with higher values in higher latitude, that are consistent very well with the direct estimation of the propagation speeds using the first order polynomial fit to the peaks of isopycnal displacement. Using the coherence spectral analysis, the mean propagation speed of 40–85–m bandpassed σ_θ observation data between Chicama and Callao was estimated to be 0.87 m s^{-1}, consistent with those estimated using reanalysis. These findings underscore how large-scale climate variability, through coastal-trapped-Kelvin waves propagation and subsequent PCUC intensification, significantly modulates the subsurface eddy activity in the Peruvian EBUS.

Keywords : Subsurface anticyclonic eddies, Puddies, Peru-Chile Undercurrent, ENSO.

---

1) Graduate School of Marine Science and Technology, Tokyo University of Marine Science and Technology, Tel: +81–80–8372–2291, email: gandy.rosales@gmail.com
2) Department of Ocean Sciences, Tokyo University of Marine Science and Technology, Tel: +81–3–5463–0460 , email: tnagai@kaiyodai.ac.jp
3) La Molina National Agrarian University, Faculty of Fisheries. Tel: + 51–999–979–988, email: licochea@lamolina.edu.pe
＊Corresponding author:
Gandy Maria ROSALES QUINTANA
(gandy.rosales@gmail.com)

1. Introduction

The Peru-Chile Undercurrent (PCUC) is a subsurface poleward flowing current that runs along the coasts of Peru and Chile. Previous studies reported that the PCUC is sourced primarily by the southern branch of the Equatorial Undercurrent (EUC) (Lukas and Firing, 1984; Toggweiler et al., 1991; Rosales Quintana et al., 2021). The influence of the EUC is intensified especially when warm events or El Niños occur (Rosales Quintana et al., 2021). Under neutral El Niño southern oscillation (ENSO) conditions, the EUC's contribution to the PCUC is minimal. Instead, the primary and secondary Equatorial Countercurrents at around 8°S and 10°S appear to play a more substantial role (Montes et al., 2010).

Several studies pointed out that the PCUC, when flowing over abrupt topographic features, initiates the formation of subsurface eddies (Contreras et al., 2019; Thomsen et al., 2016). When the PCUC generates potential vorticity (PV) with a sign opposite to the background values at the sloping bottom boundary, submesoscale instabilities, such as centrifugal and symmetric instabilities, can be triggered, leading to intense microscale turbulence. This turbulent mixing adjusts PV to a neutral value, often resulting in subsurface eddies characterized by lenses of near-zero PV water that detaches from the slope as anticyclones. These subsurface anticyclones and cyclones tend to be highly coherent and initially form at small submesoscale, commonly referred to as submesoscale coherent vortices (SCVs) (Molemaker et al., 2015; Thomsen et al., 2016). SCVs, often being nutrient-rich and dominated by anticyclones in the subsurface layers, frequently coalesce into larger mesoscale subsurface eddies (Molemaker et al., 2015). Identified in several eastern boundary upwelling systems (EBUS), these subsurface anticyclonic eddies are commonly named after the undercurrents that generate them, such as Cuddies (California Undercurrent Eddies) and Puddies (Peru-Chile Undercurrent Eddies). Furthermore, surface eddies within EBUS are known to play a role in transporting nutrients offshore and dark subsurface layers, leading to a reduction in primary production (Gruber et al., 2011). They have been found to significantly influence the heat budget, likely providing feedback to the tropical Pacific climate system by influencing sea surface temperatures, thus affecting large-scale winds over timescale consistent with ENSO (Toniazzo, 2010; Colas et al., 2012; Takahashi and Dewitte, 2016). A study by Conejero et al. (2020) demonstrated that the interannual variability in the kinetic energy of surface eddy is mainly associated with strong Eastern Pacific El Niño events, which intensify mesoscale activity off Peru, while Central Pacific El Niños showed minimal influence. Although subsurface eddies have widely been recognized within EBUS, their main characteristics and interannual variation, especially under extreme events such as El Niño still have received much less attention compared to their surface counterparts (Chaigneau et al., 2008; Chelton et al., 2011; Espinoza-Morriberón et al., 2019).

Combes et al. (2015) employed a ROMS model at 1/12° resolution to study eddies and Puddies, revealing a strong correlation between intrathermocline eddies (ITEs), or Puddies, and the ENSO equatorial signal. Their study found an inverse relationship between PCUC transport and the volume of coastal waters transported by Puddies with fewer Puddies forming during El Niño. However, this counterintuitive mechanism linking decreased Puddy formation with intensified PCUC transport during El Niño still remains elusive. In contrast, Conejero et al. (2020) reported that the subsurface EKE at 200 m depth

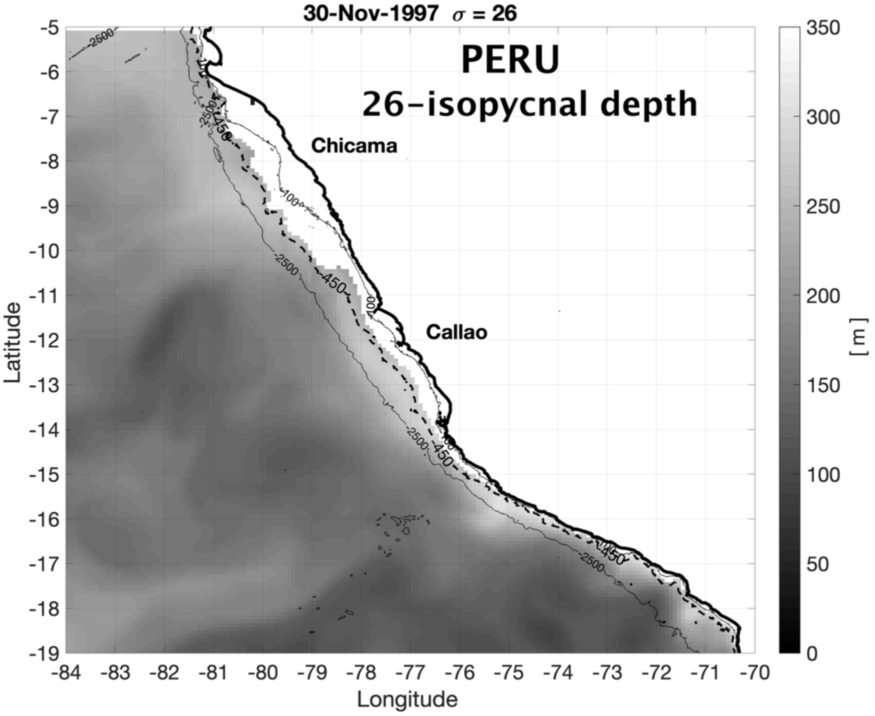

Fig. 1 Map of the Peruvian coast, showing Chicama (7.8°S - 79.7°W) and Callao (12 °S - 77.3°W) observational stations location, and the 450 m isobath along the coastline. Background shows a snapshot of σ_θ= 26 isopycnal depth for Nov 30th, 1997. Shading indicates deepening of the isopycnals from shallow (black) to deeper layers (white).

increases from northern Peru to central Chile during Eastern Pacific El Niño events (see Fig. S9 in Conejero *et al.* 2020), similar to Espinoza-Morriberón et al. (2017) that found an increase in the surface EKE off the Peruvian coast during El Niño. While heightened PCUC transport and increased subsurface EKE during El Niño imply an uptick in subsurface eddy activity, the precise nature of this subsurface eddy modulation in response to ENSO remains uncertain. In this study, we used high-resolution reanalysis data and observations to investigate subsurface eddy characteristics and behaviour.

Our objectives are to (1) elucidate the spatio-temporal variability of subsurface eddy activities in response to ENSO, and (2) explore the underlying mechanisms driving these variations.

2. Data

2.1. Observation data

We used temperature and salinity data obtained from the Peruvian Sea Institute (IMARPE) (https://repositorio.imarpe.gob.pe), covering the period from 2015 to 2020. Observations were conducted at two fixed stations along the Peruvian coastline at Chicama station (7.8°S - 79.7°W) and Callao (12°S - 77.3°W), as shown in Fig. 1. Data were recorded at 1-meter intervals from the surface down to a depth of 100 meters. Sampling occurred at least twice a month with a maximum of 15 observations per month.

2.2. Reanalysis data

We used the 1/12° resolution GLORYS12V1 reanalysis dataset from the Copernicus Marine Environment Monitoring Service (CMEMS) (https://data.marine.copernicus.eu/products). This product (product ID: cmems_mod_glo_phy_my_0.083deg_P1D-m) provides daily data from January 1993 to December 2019, including zonal (u) and meridional (v) velocity components, temperature, and salinity at depths from the surface to 5728 m, and sea surface height data (LELLOUCHE *et al.*, 2018). The dataset is based on the Nucleus for European Modelling of the Ocean (NEMO) model version 3.1 and incorporates data assimilation from in-situ and satellite observations, making it suitable for mesoscale ocean dynamics studies.

In this study, our focus is on the southern Peruvian coastal region (within 10°S-18. 5°S and 70°W-84°W). However, we also explore the northern region (north of 10°S) for computing the phase speed of the coastal trapped waves. GLORYS12V1 data set reproduces well the observational data off Peru. We compared the temperature section at Chicama and Callao (Fig. 2), from where it can be seen almost the same patterns for the isopycnals of 25.5 and 26 (solid and dotted lines respectively), and intensity. For instance, during the first trimester of 2016 at Chicama, the isopycnal of 25.5 deepened significantly in both reanalysis and observations, to later became shallower at the end of 2016. Similarly, during early 2017, observational temperature increased, reaching values close to 28℃ and 21℃ at Chicama and Callao, respectively, that was well represented by reanalysis data in both stations. To statistically validate the reliability of the reanalysis data in representing well the observation, we used the annual and seasonal Taylor diagrams comparing density profiles from Chicama and Callao stations (Fig. 2). Annual reanalysis data shows very good agreement with the IMARPE observations (r_{callao}= 0.97 , $r_{chicama}$ = 0.99), with slightly higher variance than IMARPE (normalized standard deviation = 1.25) for both stations. Seasonal comparison showed the highest correlation during austral winter season at Callao station, and summer and autumn at Chicama station.

Furthermore, we define the surface layer as the layer within the upper 50 meters, while the subsurface layer is defined as the layer within isopycnals of σ_θ = 26–26.5 kg m^{-3}, this is to capture the subsurface eddies originated from the poleward Peru Chile Undercurrent which can be identified off Peru within the isopycnals of 25.5–26.5 (ROSALES-QUINTANA et al. 2021), and to avoid influence from the surface. The locations of the observational and reanalysis data in this study are represented in a map in Fig. 1.

3. Methodology

3.1. Eddy kinetic energy

The eddy kinetic energy was computed separately for the surface and subsurface layers using Eq. (1).

$$\mathrm{EKE}=\frac{1}{2}\left(u'^2+v'^2\right), \quad (1)$$

where u' and v' are fluctuating zonal and meridional velocity, respectively, calculated by subtracting the mean velocities throughout the record from instantaneous velocities. To accurately map the spatial pattern of subsurface EKE that is caused only by subsurface intensified eddies, we compute the subsurface EKE only when that exceeds the surface averaged EKE (hereafter as the “subsurface-intensified EKE”). This allows us to avoid averaging surface intensified EKE caused by surface eddies that penetrate deep into the subsurface layer. On the other hand, sur-

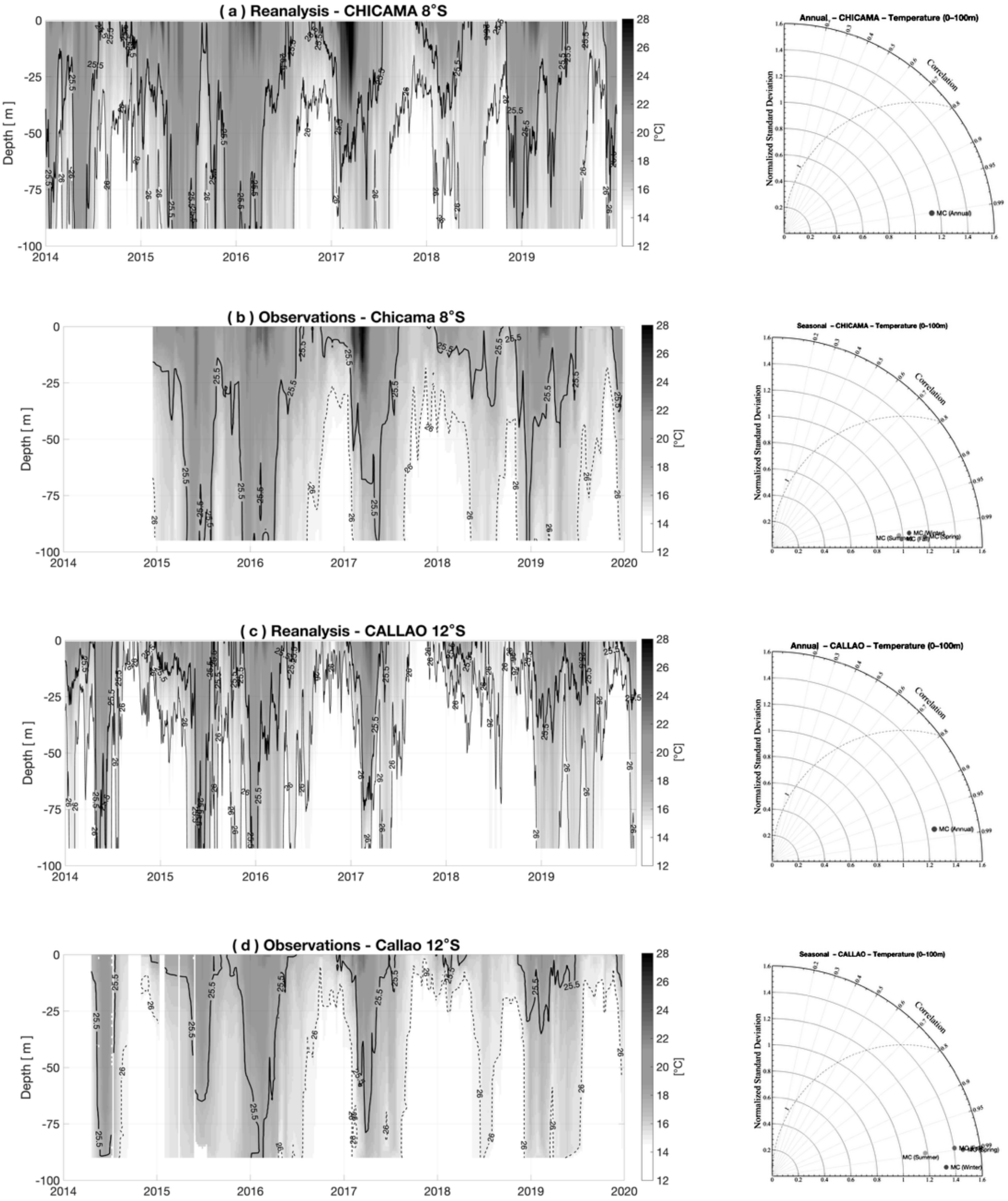

Fig. 2 Temperature section comparison for reanalysis and observations at (a,b) Chicama (8°S) and (c,d) Callao (12°S) stations from 2014 to 2019. Solid and dotted lines emphasize the isopycnals of 25.5 and 26.0 respectively. Reanalysis data is shown as daily samples, and observations with a maximum of 15 samples per month. Right column panels are the Taylor diagram for annual and seasonal comparisons between datasets.

face EKE is averaged within the top 50 m regardless of whether it is higher or lower than the subsurface layer, that is, surface EKE could also be affected by subsurface intensified eddies. To capture seasonal variations, EKE was averaged for austral summer (December to February), autumn (March to May), winter (June to August) and spring (September to November) over the period from 1993 to 2019. To investigate interannual variability, the monthly mean EKE was calculated over the same period.

3.2. Eddy identification and tracking

For eddy identification, we utilize the Okubo-Weiss (OW) parameter, defined as Eq. (2) which distinguishes rotating flows ($OW<0$) from the deformation regime ($OW>0$) (Okubo, 1970; Weiss, 1991), following a method similar to Nagai et al. (2015), previously applied for the California EBUS.

$$OW=4\left[\left(\frac{\partial u}{\partial x}\right)^2+\frac{\partial v}{\partial x}\frac{\partial u}{\partial y}\right], \quad (2)$$

where u and v are the zonal and meridional velocities, and x and y are the zonal and meridional coordinates. The eddy detection criteria involved searching for closed OW contours at -2×10^{-11} (s^{-2}). Cyclonic and anticyclonic eddies were distinguished according to the average vertical component of relative vorticity ζ within the detected eddy as in Eq. (3),

$$\zeta=\frac{\partial v}{\partial x}-\frac{\partial u}{\partial y}\ , \quad (3)$$

In the Southern Hemisphere, cyclonic eddies have $\zeta<0$, indicating clockwise rotation, whereas anticyclonic eddies have $\zeta>0$. Surface eddy detection used OW values averaged over the top 50 m, while subsurface eddy detection used OW values within σ_θ = 26–26.5 kg m^{-3}. Surface eddies were identified only when the absolute OW value averaged in the surface layer within an eddy is higher than that in the subsurface layer, while subsurface eddies are required to have both higher absolute OW values and relative vorticity within the subsurface density layer than that of the surface layer. The upper limit of the equivalent eddy radius, computed from the area within the eddy, is 200 km to extract mesoscale eddies. Also, to ensure that the detected features are true eddies and not filament-like structures, we employed a criterion for the aspect ratio (0.95–1.2). The eddies were then tracked by comparing the areas of the eddy shared between two consecutive time steps, retaining only those that lasted longer than 10 days. As mentioned in the Introduction, Puddies are originated from the PCUC. However, the eddy detection and tracking employed in the present study are not perfect to search the eddy origin. In some cases, detection fails due to the temporal evolutions of the eddies that prevent the continuous tracking, making it difficult to trace back the eddy origin. Furthermore, as the reanalysis is assimilated with the observation data, that do not necessarily capture the entire history of the subsurface eddies, the search for the origin of the subsurface eddy would be not feasible. On the other hand, our analyses for the subsurface layer are conducted within the density range σ_θ= 26–26.5 kg m^{-3}, which does not outcrop except very near the coast, excluding the possibility of the subsurface eddies caused by subduction processes. Accordingly, although our eddy detection and tracking have these limitations, we consider all the detected and tracked subsurface anticyclones as Puddies.

For each tracked eddy, the eddy non-linearity parameter is defined as the ratio of the swirl velocity U to the eddy propagation velocity c, U/c, which is obtained as averaged value based on our eddy tracking results for each layer (the same c = 0.034 m s^{-1} is found for each layer).

Where *U/c > 1* suggests that the feature is nonlinear and maintains its coherent structure during their propagation (FLIERL, 1981) and capable of trapping matters inside and travelling with them.

3.3. Phase speed estimation

3.3.1. Vertical mode and speed of internal Kelvin wave for reanalysis data

To investigate the phase speed (C_p) of the internal Kelvin wave, linearized equations for along shore momentum, vertical momentum, density conservation, and continuity are combined into one equation for the vertical velocity.

$$\frac{\partial}{\partial t^2}\left(\frac{\partial^2 w}{\partial z^2}\right)+\left(\frac{\partial}{\partial t^2}+N^2\right)\frac{\partial^2 w}{\partial x^2}=0, \quad (4)$$

where $N^2=-g\left(d\bar{\rho}/dz\right)/\rho_o$ is the square of buoyancy frequency, g is the gravitational acceleration, with $\bar{\rho}$ (z) as the laterally averaged density and ρ_o as the constant density. Here, we assume flat bottom and coast as a vertical wall, no cross-shore velocity, considering the Boussinesq approximation. Assuming a following wave solution for vertical velocity w of variable separation type, $w=W\,(z)\sin\,(kx-\omega t)$, where k is along-shore wavenumer, ω is the frequency, and t is the time in Eq. (4), the vertical mode equation for the internal Kelvin wave induced vertical velocity can be obtained in the Sturm-Liouville system (Eq. (5)).

$$\frac{\partial^2 W}{\partial z^2}+\left(\frac{N^2-\omega^2}{c_p^2}\right)W=0 \quad (5)$$

Daily buoyancy frequency square N^2 along 450 m isobath as a function of depth, latitude and time is computed only during El Niño events. Then, the obtained buoyancy frequency is used to solve (Eq. (5)) for each water column numerically with arbitrary k as an input parameter and the boundary conditions for $W\,(z)=0$ at the surface $z=0$ and the bottom $z=450$ m. The obtained eigenvalues, λ_i provide wave frequencies square ω^2, for each mode i. Therefore, wave phase speeds C_p for each mode i can be obtained by $\sqrt{\lambda_i}\,/k$. The eigenfunction represents a vertical structure of the vertical velocity.

3.3.2. Estimation using cross correlations for reanalysis data

To assess the meridional propagation characteristics, we estimated C_p along the 450 m isobath off the coast of Peru using the σ_θ= 26 isopycnal depth fluctuations from 1993 to 2019. Specially, we focused on anomalous vertical displacements of the σ_θ= 26 isopycnal during El Niño conditions across latitudes between 5°S to 19 °S, spaced approximately 2° apart. Before computing C_p, we first isolate time periods corresponding to El Niño events, then we remove the seasonal cycle and long-term trends by subtracting the monthly climatology and detrending the signal. A Butterworth bandpass filter (4th order, 20–120 days passband) was applied to retain intraseasonal variability commonly associated with coastal trapped waves. After the preprocessing, we then compute a normalized cross-correlations between the filtered time series at a reference latitude (14°S) and all other selected latitudes. For each latitude pair, the lag corresponding to the maximum cross-correlation was identified and extracted. The spatial lag was computed based on the meridional distances between latitudes (assuming a spherical earth approximation). A linear regression was then performed between the lag in days (δt) and the spatial distance (δx), where the slope ($\eta=\delta t/\delta x$) represents the time delay per unit distance. The $\overline{\mathrm{C}\,p}$ was then computed as the reciprocal of this slope as, $\overline{\mathrm{C}\,p}=1/\eta$, and converted to meter per second.

3.3.3. Estimation using the 1st order polynomial fitting for reanalysis data

Since the reanalysis can provide data along the coast at every grid point, the speed of the

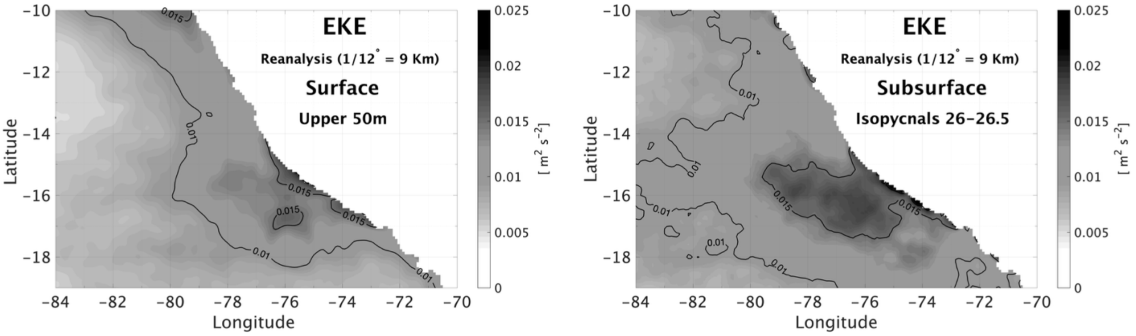

Fig. 3 Eddy kinetic energy（EKE）[$\mathrm{m}^2\ \mathrm{s}^{-2}$] spatial distribution averaged over the surface（0 to 50 m depth）and subsurface（$\sigma_\theta = 26\text{–}26.5\ \mathrm{kg\ m}^{-3}$）layers for the period 1993–2019. The subsurface EKE values were included in the average only when they exceeded the surface EKE.

propagating signal can be estimated more directly than observation data at a few locations. Therefore, C_p was estimated by analysing alongshore transects of the $\sigma_\theta = 26$ isopycnal depth anomalies derivate from reanalysis data during El Niño events. For each selected event, time-distance diagrams were constructed by plotting $\sigma_\theta = 26$ isopycnal depth fluctuations as a function of distance along the Peruvian coastline and time, enabling the visualization of propagating internal signals. The peak detection was performed for the isopycnal depth. Peak points connected clearly that implied propagating signal, were manually extracted from the time-distance diagrams. Subsequently, a first-degree polynomial fit was applied to each segment of the selected peaks. The slope of the fitted line provided an estimate of the C_p. To capture spatial variability of C_p, the obtained C_p was bin-averaged as a function of latitude.

3.3.4. Estimation using coherence analysis for observational data set

For observational data in Chicama（7.8°S）and Callao（12°S）（IMARPE）, we selected the period that has continuous approximately weekly data from 2015 through 2020 in 40–85 m depth, avoiding influences from the surface. To isolate propagating waves signals as previously applied to reanalysis data, we use a fourth-order Butterworth banpass filter to each time series, with a filter designed to retain variabilities within the period of 20–120 days to investigate coastal trapped Kelvin waves（CAMAYO and CAMPOS, 2006; DEWITTE et al., 2012; BELMADANI et al., 2012; POLI et al., 2022）. The phase lag, $\delta\theta$ was extracted in the frequency ranges where coherence square is higher than 0.15, which then used to compute time lags, δt by $-\delta\theta/(2\pi\omega)$. The phase speed C_p can be obtained by $\delta x/\delta t$, where δx is the great-circle distance between Chicama（7.8°S）and Callao（12°S）.

4. Results

4.1. Eddy Kinetic Energy

Surface EKE exhibits large values within 200–300 km of the coast, with slightly elevated levels north of 12°S and very high values south of 14°S along the Peruvian coast, consistent with previous studies（COMBES et al., 2015）(Fig. 3). In contrast, subsurface EKE shows a distinct spatial distribution, with higher values（≈ 0.02 $\mathrm{m}^2\ \mathrm{s}^{-2}$）concentrated in the southern part of the study area, and up to 0.025 $\mathrm{m}^2\ \mathrm{s}^{-2}$ restricted to the nearshore coastal area, between 14°S and 18

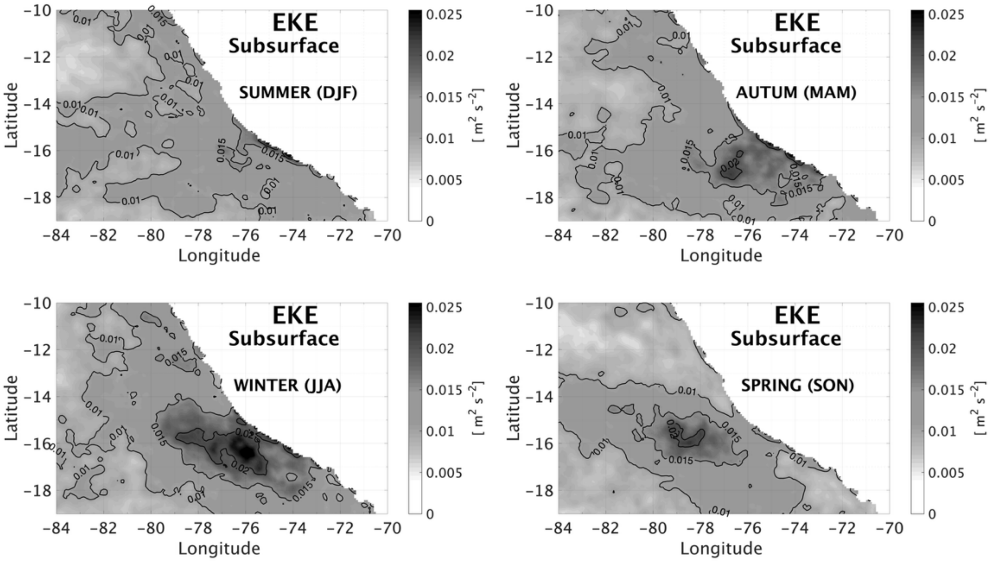

Fig. 4 Seasonal variability of the eddy kinetic energy (EKE) [$m^2\ s^{-2}$] averaged for the subsurface layer (within σ_θ = 26–26.5 kg m^{-3}) from 1993 to 2019. The subsurface EKE was averaged only when the EKE values were larger than that in the surface layer.

°S. This suggests that subsurface eddies are generated primarily in the southern region, compared to the surface eddies that can develop along the entire coastline. At the subsurface, high seasonal variability was found in the averaged EKE off the south coast of Peru. High EKE values are seen mainly during austral autumn, winter and spring with values higher than 0.02 $m^2\ s^{-2}$ that are concentrated south of 14°S (being winter the highest peak), while during austral summer, EKE showed its lowest values in the same region (Fig. 4). These changes in EKE seem to be synchronized with the seasonal variability of the PCUC, which intensifies from autumn to the beginning of winter. FLORES et al. (2013) used the 15℃ isotherm depth as an indicator of the PCUC and its variability off Peru. They showed that when the PCUC intensifies, the 15℃ isotherm deepens up to 250 m during the austral autumn. In contrast, during the austral spring, the PCUC weakens, resulting in a shallower 15℃ isotherm. Such behaviour is similar to that observed in the equatorial Pacific, where the EUC strength is tightly linked to the thermocline depth variability (KESSLER et al., 1995). Our eddy detection and tracking results (in section 3.2) align well with the EKE enhancement during the austral autumn and winter seasons, showing an increase in the number of detected subsurface eddies, particularly subsurface anticyclones, Puddies. This implies a strong link between the seasonal variability of the PCUC and the formations of the subsurface eddy.

4.2. Eddies detected off Peru

To better understand how the subsurface eddies modulate interannually and how they can be linked to EKE variations, we analysed 27 years of reanalysis data and used eddy detection and tracking techniques. Consistent with the findings of COMBES et al. (2015), our results show that surface intensified cyclones (56%) are more

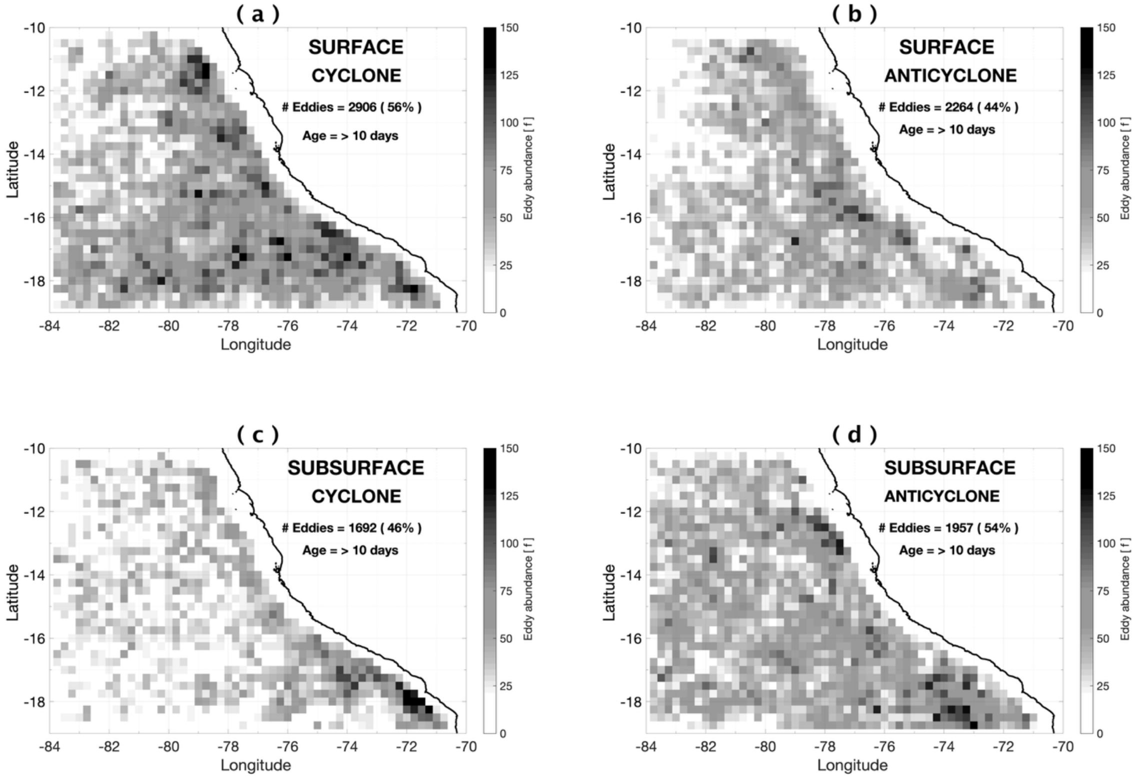

Fig. 5 Abundance of surface and subsurface detected and tracked eddies that lived longer than 10 days for (a) surface cyclones, (b) surface anticyclones, (c) subsurface cyclones and (d) subsurface anticyclones. For counting eddies, we consider the eddy that lasted longer than 10 days from the time it is born and followed it until it dies. We represent the cumulative count of daily eddy appearance for 27 years, within a grid cell of 0.25°× 0.25°. The eddies found offshore are most likely originated from the nearshore within the PCUC.

abundant than anticyclones (44%) in the surface layer. In contrast, subsurface anticyclones dominate the subsurface layer, accounting for 54% of all eddies (Fig. 5). The differences in the spatial distributions detected eddies between those in the surface layers (Fig. 5 a-b) and the subsurface layers (Fig. 5 c-d) are evident. In the surface layer, cyclones are distributed in the wide region from nearshore to the offshore up to 1,200 km from the coast especially in the southern region (16–18°S), while anticyclones are mostly concentrated within 100 -600 km from the coast. In the subsurface layer, cyclones are restricted to nearshore, predominantly south of 16° S, while anticyclonic eddies exhibited localized hotspots along the coast at 12°S - 14°S and south of 16°S. In addition to spatial distributions, subsurface-intensified eddies show distinct temporal patterns. Fig. 6 shows monthly statistics, revealing that subsurface anticyclonic eddies, Puddies, are more prevalent in austral autumn (April to May) with its highest peak in April (with around 150 Puddies), followed by a second peak during austral winter (July, with 135 Puddies, Fig. 6a). Subsurface cyclones follow a similar trend with peak occurrences in May and June. Both anticyclonic and cyclonic eddies shown a marked decline in activity during the austral

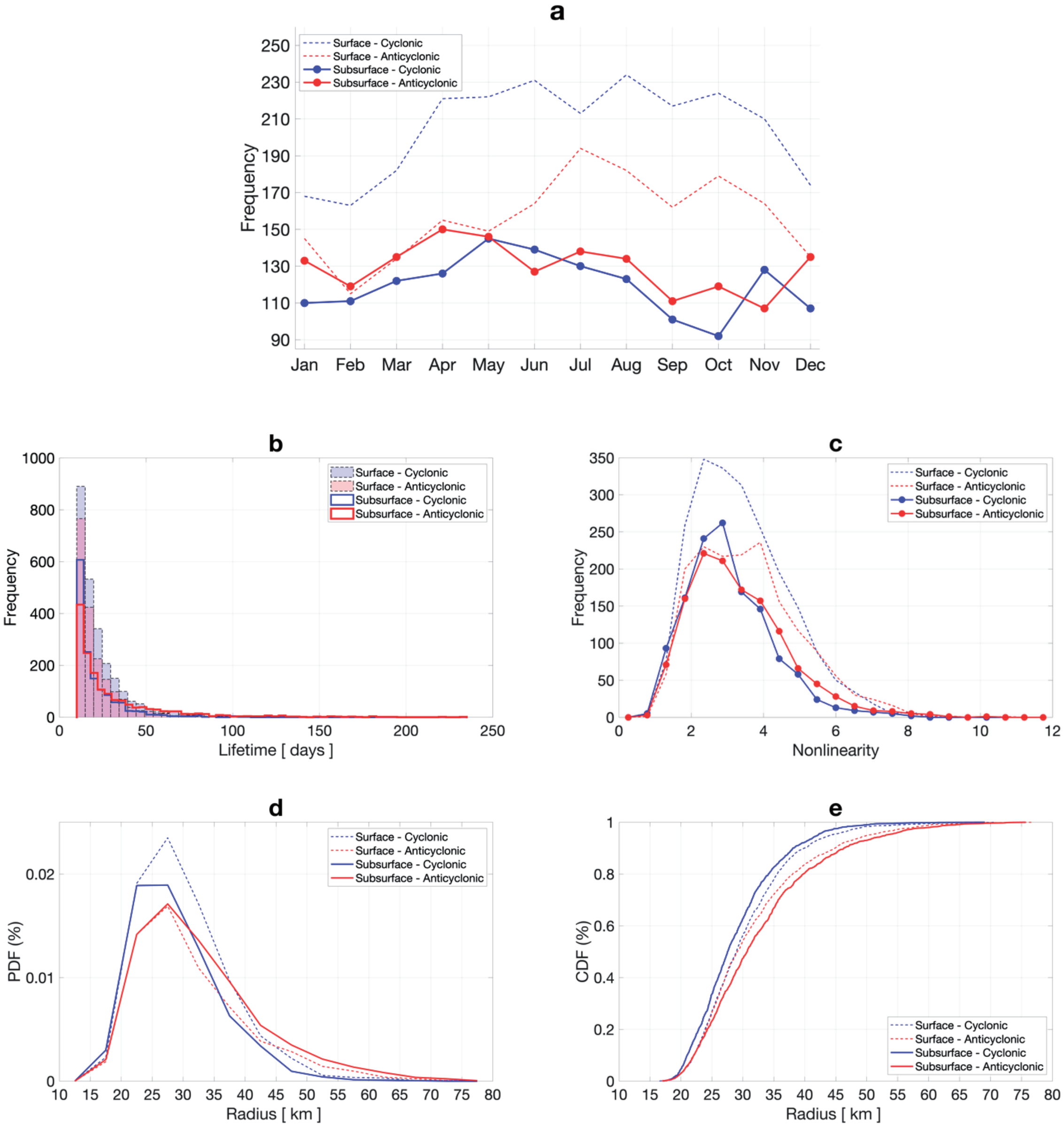

Fig. 6 Eddy statistics for detected and tracked eddies that lived longer than 10 days for (a) seasonality, (b) lifetime, (c) nonlinearity, (d) probability density function and (e) cumulative density function for radii.

spring, reaching their lowest abundance in October and November, respectively. Although the subsurface EKE shows its highest peak during winter season (Fig. 4), these subsurface eddy activities, intensified in autumn is consistent with the enhanced EKE in autumn, suggesting that subsurface eddy activities are highly consistent with the seasonal variability of PCUC (VERGARA et al., 2016). Moreover, the numbers of subsurface cyclones and anticyclones increase

Table 1. Non-linearity parameter defined as the ratio of the swirl velocity U to the theoretical propagation velocity (c = 0.034 m s^{-1}) of the eddy. Where U/c>1 suggests nonlinearity, maintaining its coherent structure during their propagation.

Eddy type	U/c	Abundance %
Surface Cyclones	3.4	56
Surface Anticyclones	3.6	44
Subsurface Cyclones	3.1	46
Subsurface Anticyclones	3.3	54

during November and December, respectively. In contrast, surface-intensified eddies showed their highest abundance mostly during austral autumn to spring (April-October).

Another notable contrast between subsurface cyclones and anticyclones is that the latter tends to have longer lifespans (Fig. 6b); some subsurface anticyclonic eddies persist for up to 245 days, while cyclones have a maximum duration of 110 days. Most subsurface eddies have radii between 25 and 30 km (Fig. 6d) with anticyclones tending to be larger than cyclones; 66% of anticyclones have radii below 35 km, while it is as high as 83% for cyclones (Fig. 6e). Moreover, we found that both surface and subsurface eddies exhibited high non-linearity (Fig. 6c), allowing them to trap and transport matter. Our results showed that surface-intensified cyclones ($U/c = 3.4$) and anticyclones ($U/c = 3.6$) have on average higher non-linearity than subsurface eddies, which showed $U/c = 3.1$ for cyclones and $U/c = 3.3$ for anticyclones. The mean non-linearity for subsurface eddies ($\overline{U/c} = 3.2$) is found to be statistically different with a 5% significance level from that for the surface one ($\overline{U/c} = 3.5$), indicating that subsurface eddies are slightly leakier than surface eddies (See Table 1).

4.3. $\sigma_\theta = 26$ isopycnal depth variability

To examine how differently El Niño events influence the subsurface eddy abundance off Peru, we utilize the $\sigma_\theta = 26$ isopycnal depth variability as a proxy for changes in the upper limit of the PCUC. The $\sigma_\theta = 26$ isopycnal depth tends to deepen during warm events, with greater southward penetration along the coast. ENSO events are commonly defined by the averaged sea surface temperature anomaly (SST) along the Equatorial Pacific at the Niños areas such as Niño 3.4 (5° N-5°S, 170°W-120°W) and Niño 1 + 2 (0°-10°S, 90°W-80°W). The latter region is particularly relevant for the South American coast. The two bottom panels of Fig. 7 show the SST anomaly for Niño3.4 and Niño 1 + 2 from 1993 to 2019, highlighting the El Niño events defined by the threshold of ± 0.5, following the definition of Oceanic El Niño index (ONI) and Coastal El Niño index (ICEN). A recent work by BERTRAND et al. (2020) has further categorized ENSO phases beyond the canonical El Niño 3.4 definition, considering the intensity of rainfall/dry conditions, and zonal location of the warm pool, which has been used in this study to define El Niño type.

During extreme (Ex) El Niño events, such as those of 1997–1998 and 2015–2016, SST anomalies in Niño 1 + 2 rose to about + 4℃, while Niño

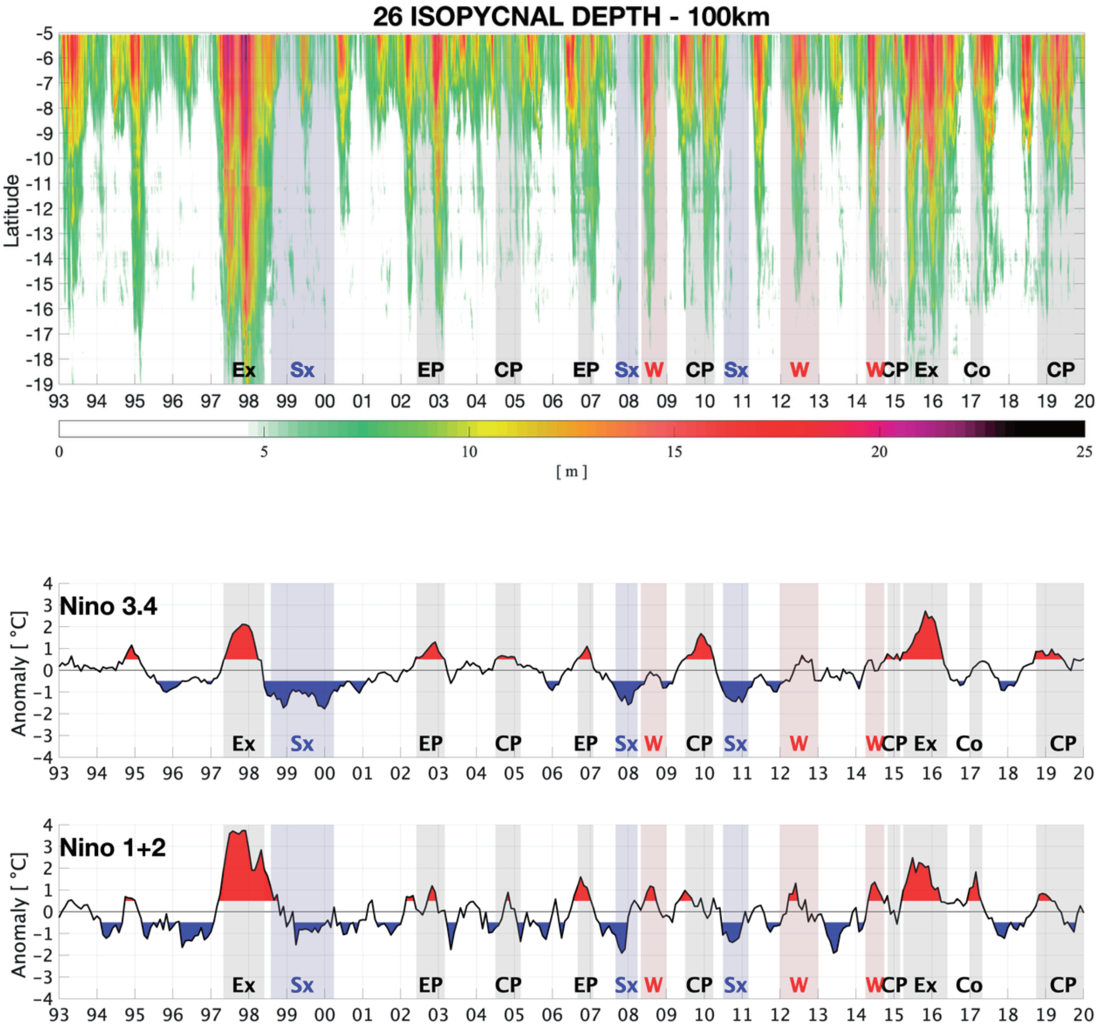

Fig. 7 Monthly averaged σ_θ= 26 isopycnal depth [m] for the 100 km distance from the coast, from reanalysis data is shown in the top panel. Shaded areas indicate ENSO phases as follow; Extreme El Niño (Ex), Eastern Pacific El Niño (EP), Central Pacific El Niño (CP), Coastal El Niño (Co), Strong La Niña (Sx), and moderately warm periods (W). Threshold of ± 0.5 is indicated with red and blue for both (middle) Nino 3.4 and (bottom) 1 + 2 indices.

3.4 anomalies reached ≈ + 2.5 ℃, corresponding to a markedly increased number of subsurface anticyclonic eddies (Puddies), as described later in section 4.5. The isopycnal depth also deepened significantly across latitudes, reaching up to 25 m of its amplitude during 1997–1998 (Fig. 7). Although both events are classified as extreme, they differed somewhat. The 1997–1998 event produced a uniform deepening of the σ_θ= 26 isopycnal from 5°S to 19°S, while the 2015–2016 event caused a more prolonged and pronounced deepening primarily in the northern latitudes (5°S to 12°S). This distinction may be partly attributed to the anomalously warm conditions preceding the 2015–2016 event (the Central Pacific El Niño 2014–2015) and to long-term background warming (SANTOSO et al., 2017).

During two eastern Pacific (EP) El Niños (e.g. 2002–2003, 2006–2007), moderate isopycnal deepening compared to extreme events are seen, with Niño 3.4 and Niño 1 + 2 anomalies generally ranging between + 0.5℃ and + 2℃. Comparing these events, the σ_θ= 26 isopycnal depth showed more pronounced deepening during 2002–2003, with a meridional extension up to 14°S (> 10 m of isopycnal deepening), while the 2006–2007 event showed a more localized deepening concentrated in the northernmost region (reaching only up to 10°S). Central Pacific El Niños (CP), such as 2004–2005, 2009–2010 and 2014–2015, primarily affect the central equatorial Pacific and inducing weaker and more localized changes in isopycnal depth along the Peruvian coast. Previous studies pointed out that CP events are less related to the thermocline variations and that their variability might be more influenced by atmospheric forcing (KAO and YU, 2009; SANTOSO et al., 2017). On the other hand, Ex and EP events are associated with basin-wide thermocline and wind variations. The σ_θ= 26 isopycnal in Fig 7 showed a very weak deepening during CP 2004–2005 and 2014–2015 with values between 5–13 m, that is different from CP 2009–2010 with deeper variability (up to 20 m of isopycnal deepening) limited to the northernmost region. Coastal El Niño (Co) events, exemplified by the 2017 event, caused a very short in time and highly localized isopycnal deepening of ~15 m near the northern Peruvian coast (5°S to 8°S). These events, unique to the Peruvian upwelling system, are driven by regional atmospheric and oceanic processes rather than basin-wide conditions, with impacts confined to the nearshore regions (RAMÍREZ and BRIONES, 2017). We also defined moderately warm (W) periods (i.e., 2008–2009 2012–2013, early 2014) marked by positive SST anomalies in Niño 1 + 2 (Fig. 7), although they never fully developed into classical El Niño conditions (SU et al., 2014), nor classified as El Niño events, these warm periods still appear to influence the isopycnal depth and likely contribute to increased subsurface eddy formation. Strong La Niña (Sx) events (1999–2000, 2007–2008, 2010–2011) lead to significant shoaling of the isopycnal (Fig. 7) and are associated with enhanced upwelling, cooler subsurface waters, and increased productivity along the coast. During these extremely cold periods, we observed a corresponding negative trend in subsurface eddy formation as described in section 4.5.

4.4. Interannual variability of EKE

We previously demonstrated that changes in the depth of the σ_θ= 26 isopycnal are synchronized with the onset of warm events. We now explore whether this relationship also appears in the eddy kinetic energy (EKE). The average EKE within the first 100 km from the coast (Fig. 8) showed pronounced meridional variability, with elevated values observed primarily in two latitudinal bands: from 5°S to 11°S, and from 14°S to 18°S, in both the surface and subsurface layers. Over time, changes in EKE correspond well to the deepening of the σ_θ= 26 isopycnal. At the surface, EKE notably intensifies during the two extreme El Niño events (Ex) 1997–1998 and 2015–2016. In Ex 1997–1998, enhanced EKE was widespread throughout the entire meridional range, while in Ex 2015–2016 the increases were pronounced over time but concentrated in the region north of 11°S. On the other hand, EP events showed moderate EKE confined to the northernmost region (2006–2007) or spread separately within the northernmost and southernmost regions (2002–2003). But for the subsur-

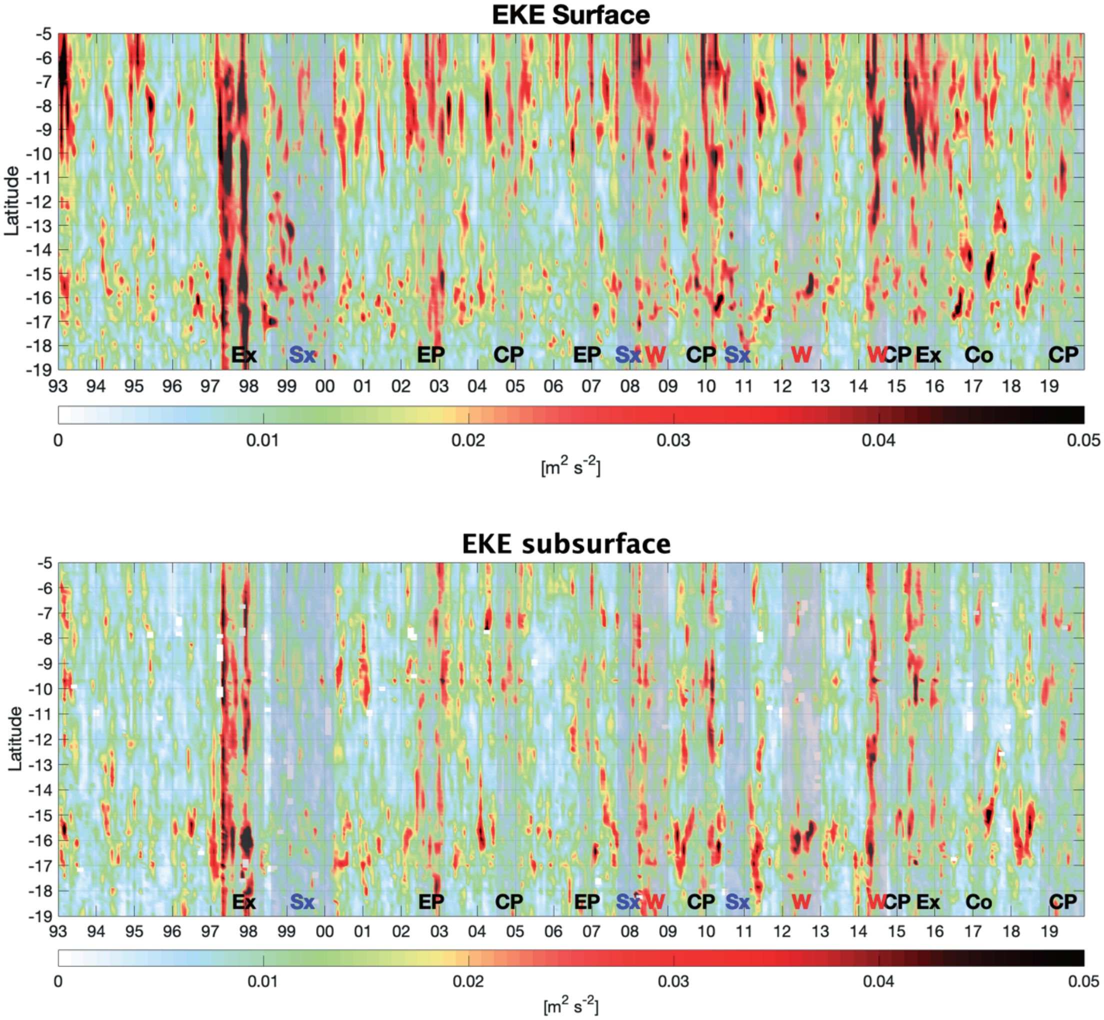

Fig. 8 Spatial-temporal variability of the monthly averaged eddy kinetic energy (EKE) [$m^2\ s^{-2}$], for the surface (upper 50 m depth) and subsurface (within σ_θ= 26–26.5 isopycnal) layers within the first 100 km from the coast. EKE varies along latitudes from 5°S to 19°S, and years from 1993 to 2019. Shaded areas indicate ENSO phases as follow; Extreme El Niño (Ex), Eastern Pacific El Niño (EP), Central Pacific El Niño (CP), Coastal El Niño (Co), Strong La Niña (Sx), and moderately warm periods (W).

face layer, EP events exhibit much less EKE of 0.03 - 0.04 $m^2\ s^{-2}$ than that in the surface layer. Even if the EKE increases, it is rather patchy and limited to the southernmost region, south of 14°S. EKE during Central Pacific El Niños (CP) were mainly enhanced in the surface layer and restricted to the northernmost region, while CP events did not show a clear enhanced EKE in the subsurface layer. We define moderately warm periods (W) in which temperature ranges ± 0.5℃, such as 2008–2009, 2012 and 2014, that were also characterized by elevated EKE restricted mostly to the northernmost region at the surface layer, and to the southernmost region at the subsurface layer (south of 14°S), expect for 2014 that showed continuous enhancement in EKE along the entire region from 5°S to 19°S. The 2017 Coastal El Niño (Co), showed similarly enhanced EKE in the surface and subsurface layers, which was, however, not as strong as the other warm events (i.e. Ex, EP and W events) and limited to the region between 5°S to 8°S for both layers. On the other hand, strong La Niña (Sx) events were marked by very low subsurface EKE, deviating from the patterns observed in the surface layer where EKE did not completely vanish. The EKE variations during strong La Niña (Sx) events are consistent with a negative trend in the number of subsurface eddies detected during the same events (as described in section 4.5).

These results imply that the formation of subsurface eddies is more vigorous during most types of the El Niño, and they are highly weakened during La Niña events, suggesting that ENSO-related variability is likely to exert a strong influence on subsurface eddy activities off Peru.

4.5. Interannual variability of the eddies detected off Peru

We have shown that the $\sigma_\theta = 26$ isopycnal depth and subsurface EKE increased during warm events. Here, we examine whether this was reflected in the number of eddies detected in the subsurface layer and compare that to the surface counterpart (Fig 9). The surface and subsurface eddies detected and tracked off Peru exhibited substantial interannual variations that would be influenced by ENSO events. During Ex 1997–1998 and 2015–2016, numbers of tracked subsurface anticyclonic eddies, Puddies, showed marked increases with up to 6 eddies generated per month (Fig. 9b), while, for the latter Ex event, the number of subsurface cyclones were also increased as much as subsurface anticyclones. In the surface layer, the number of anticyclones were always lower than cyclones (Fig 9a). During EP 2002–2003 and 2006–2007 events, the number of subsurface eddies especially subsurface anticyclones showed a decreasing tendency, leading to more abundant subsurface cyclonic eddies than subsurface anticyclonic eddies. Differently, during CP events, the number of subsurface anticyclones was always higher than cyclones, except for CP 2009–2010 where the number of subsurface anticyclones showed a peak but with decreasing tendency. On the other hand, in the surface layer, cyclones surpassed anticyclones during all CP events. During Co 2017 event, subsurface eddies, both cyclones and anticyclones showed peaks of up to 7 eddies for a month, that are different from the surface eddies. Moderate warm periods (W) persistently showed elevated number of subsurface eddies, with the highest peak in 2008–2009 event in both layers. In the surface layer, W events exhibited higher number of eddies during 2008–2009 and 2014–2015 (Fig. 9a). During strong La Niña (Sx) events (1999–2000, 2007–2008, 2010–2011), the number of subsurface eddies exhibited a decreasing tendency compared to the previous year especially for subsurface anticyclones. Within Sx events, the tendency shows decreasing number of subsurface anticyclones followed by an increase near the end of the events with the highest increase happened during 2007–2008.

A scatter plot between averaged isopycnal depth at $\sigma_\theta = 26$ from 10–19°S and numbers of subsurface eddies suggests that the abundance of subsurface eddies (both cyclones and anticyclones) showed weak statistically significant positive correlations with the isopycnal depth ($r = 0.17$, $r = 0.26$, respectively, p-value < 0.05, in Fig 10), while the correlations are statistically not-

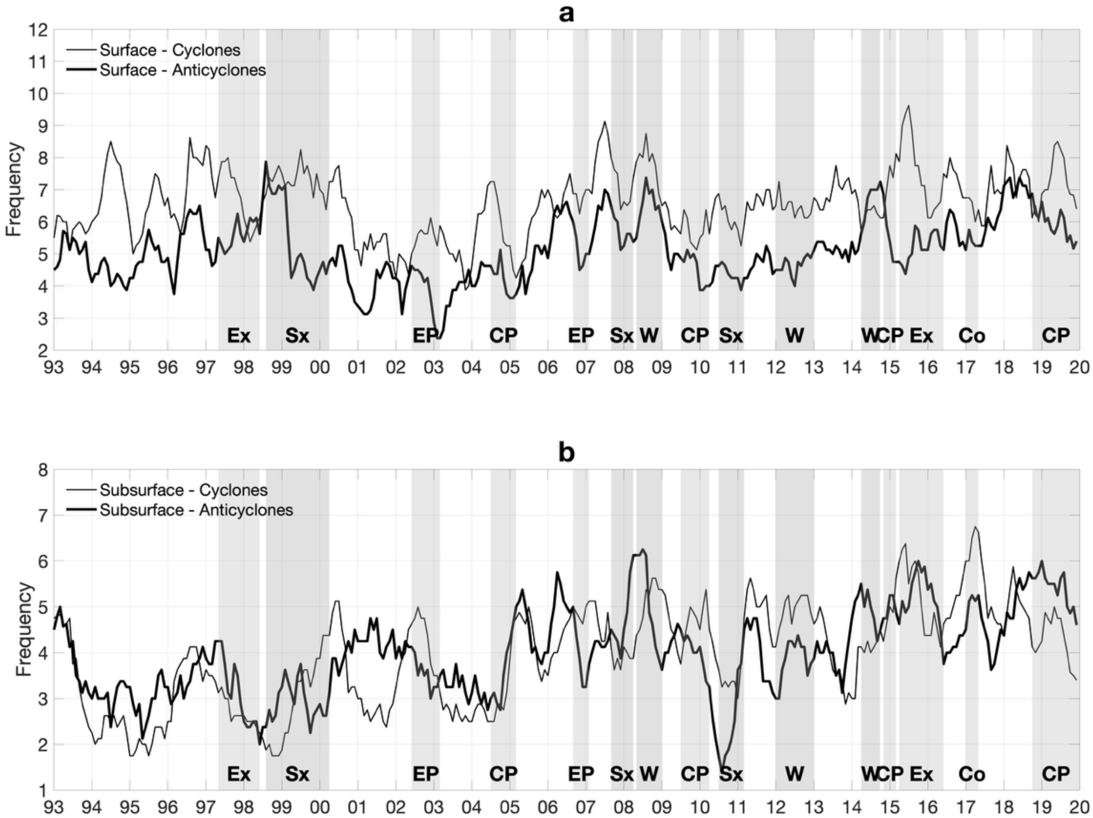

Fig. 9 Interannual variability of the number of eddies detected and tracked during 1993 to 2019 off Peru at both surface (a) and subsurface (b) layers. Shaded areas indicate ENSO phases as follows; Extreme El Niño (Ex), Eastern Pacific El Niño (EP), Central Pacific El Niño (CP), Coastal El Niño (Co), Strong La Niña (Sx), and moderately warm periods (W). Note that y-axis for the number of eddies differ for each layer. For both panels, "frequency" refers to the number of eddies born within a month, counting those eddies that lived at least 10 days (e.g. Eddy1 was born in day 1 and lived 30 days in total, then this eddy is count as "1" for this birth month).

significant for surface eddies. This indicates that when the isopycnal deepens, it appears to have influence on the formation of subsurface eddies.

In the surface layer, cyclones dominate almost constantly over anticyclones (Fig. 9a). However, the trend of number of cyclone and anticyclones does not always synchronize. During the EP of 2002–2003, cyclones exhibited a small peak, while anticyclones decreased, demonstrating an opposite trend. After these events, surface-layer cyclones and anticyclones generally showed similar tendencies over the years. Furthermore, in both the surface and subsurface layer, we identified a positive trend between 1993 and 2019 in the number of eddies detected, which could be due to global warming, as Conejero et al. (2020) suggested by using EKE in the surface layer. However, since this topic is beyond the scope of this study, we will leave it for future investigation.

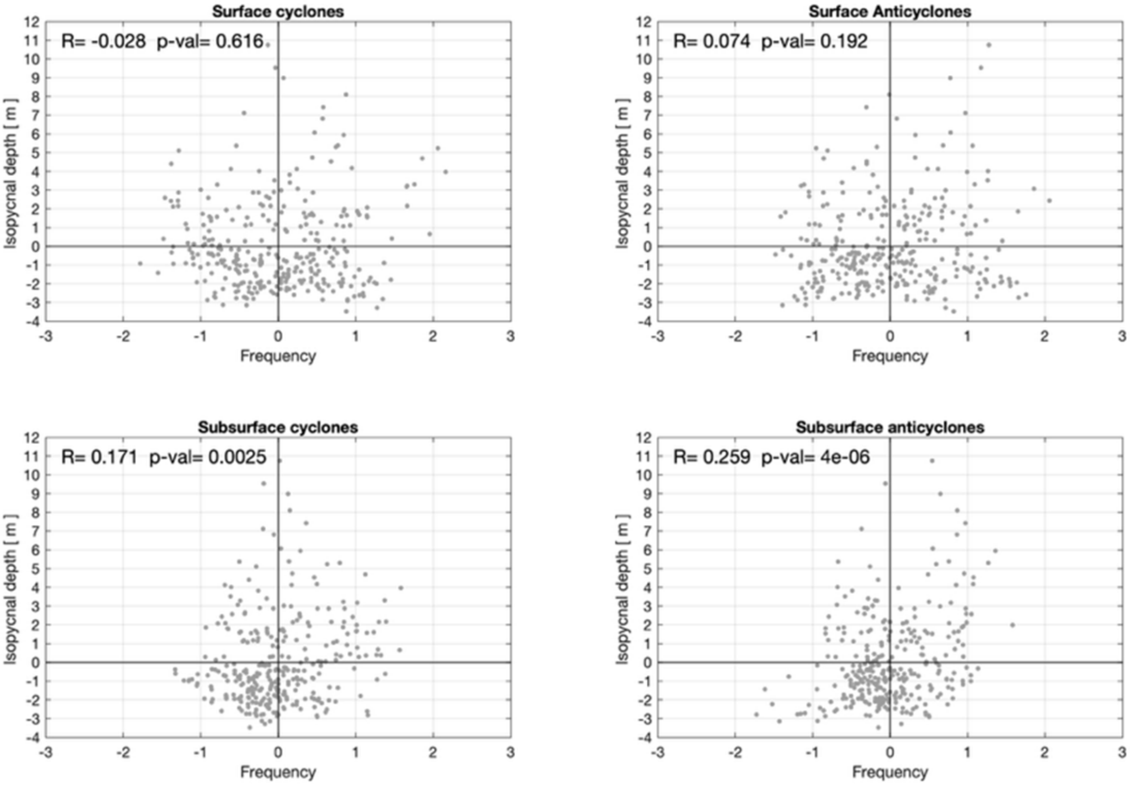

Fig. 10 Relationship between σ_θ= 26 - isopycnal depth ［m］ and eddy frequency （number of eddies born in a month） for surface and subsurface cyclones and anticyclones detected between from 1993 to 2019 within the southernmost region 10°S to 19°S are shown. A running-mean of 5 months was applied to both variables. Correlation coefficient （R） and significance （p-value） are also shown.

4.6. Coastal trapped wave propagation

Isopycnal depth along the Peruvian coast clearly responded to ENSO variability and other warm events. To further address these patterns, we investigate the possibilities of the poleward propagating coastal trapped waves by estimating the speed of the propagation, C_p in the study region using several methods. The C_p of the first baroclinic mode was estimated by solving the vertical mode equation (5) during El Niños events along the 450–m isobath （5°S-19°S） in Fig. 11. The results show distinct latitudinal variability in C_p, with notably slower propagation in the southernmost region, south of 16°S. During most of the El Niño events, C_p usually shows poleward phase speeds larger than 0.8 ms^{-1}, with a maximum C_p during Ex 1997–1998 event （1.7 ms^{-1} Fig. 11a）. On average, C_p ranged between 0.6 to 1 ms^{-1} （0.95 ms^{-1} overall, Fig. 11b） along the coast, with a general decreasing trend towards higher latitudes. The eigenfunction solution as a function of latitude and σ_θ （Fig. 11c） showed maximum amplitude near σ_θ = 26 kgm^{-3}, suggesting that our choice of the isopycnal to detect the propagation was reasonable although the maximum amplitude shifts denser layer southward. The strong latitudinal dependence suggests significant regional differences in baroclinic wave dynamics during El Niño years. We compared these results with the estimates of C_p

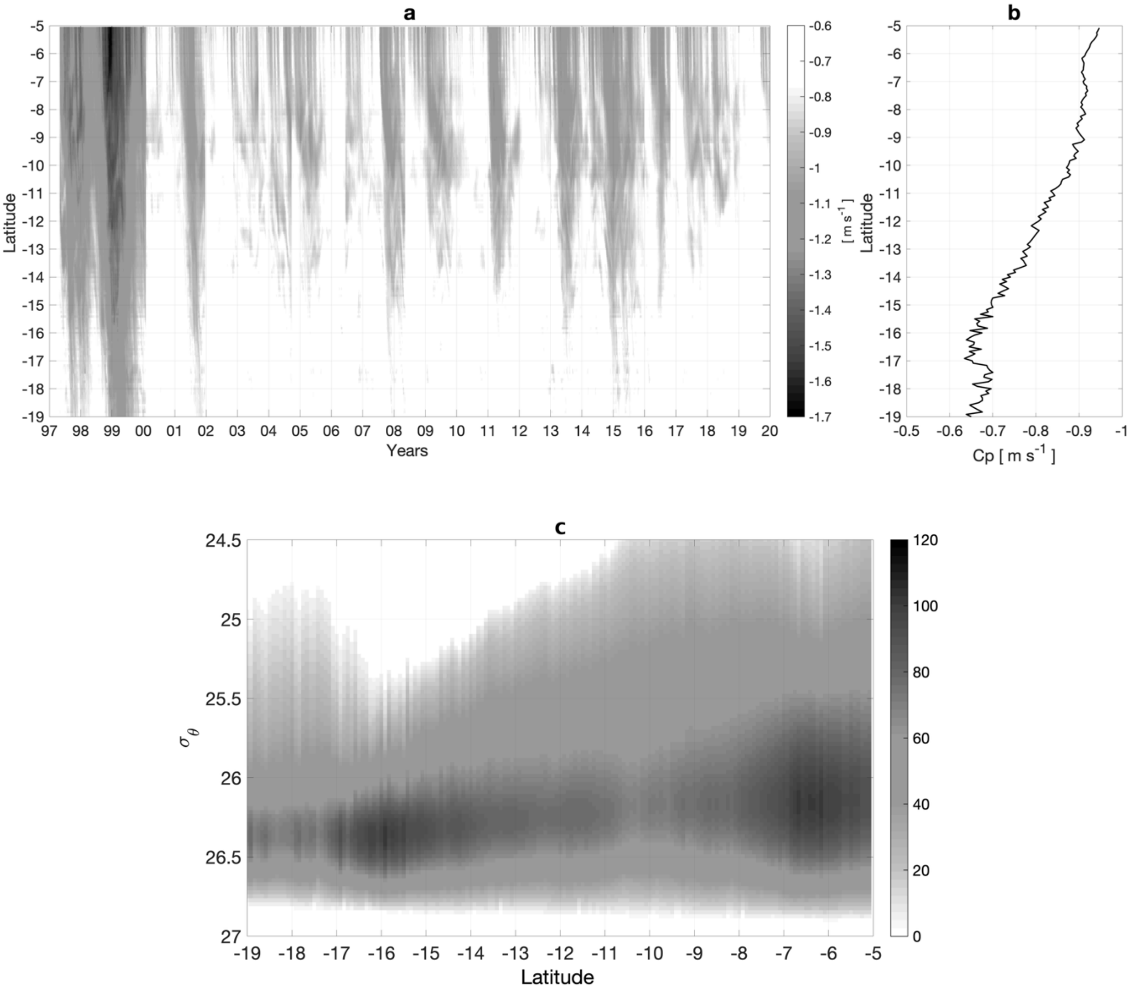

Fig. 11 (a) Phase speed (C_p) calculated from the first baroclinic mode between 1993 to 2019 and the (b) averaged C_p [ms^{-1}] across latitudes. (c) Eigenfunction of the first baroclinic mode for vertical velocity as function of density.

using the cross-correlation analysis and the 1st order polynomial least square fitting to the peaks in isopycnal deepening only during El Niño events. The obtained C_p are consistent values to the modal analysis also with the same decreasing trend for higher latitudes. Overall C_p calculated from cross-correlations resulted in 1.2 ms^{-1}, while C_p ranged between 0.5 ms^{-1} to 0.83 ms^{-1} (from south to north off Peru, Fig. 12 b) when using the 1st order polynomial least square fitting.

For observational data, coherence analysis of the band-passed anomalies of the 40–85 m-averaged σ_θ at Chicama (7.8°S) and Callao (12°S) during 2015 through 2020 in which relatively continuous data are available, revealed two distinct peaks in coherence square accompanied by positive phase lag (Fig. 13). The highest coherence peak corresponds to the fluctuation period

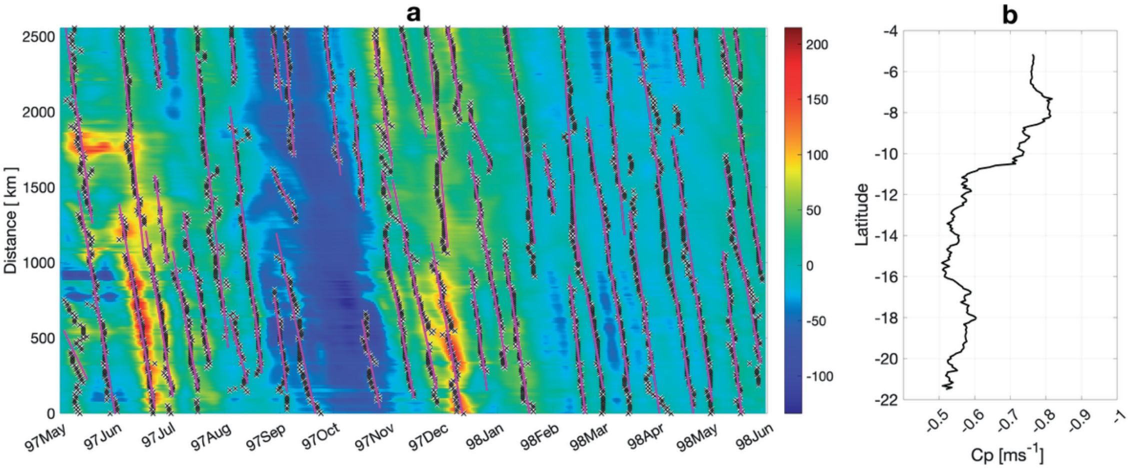

Fig. 12 Phase speed (C_p) calculated from alongshore transects for reanalysis data. (a) Point-by-point extracted data within the σ_θ= 26 isopycnal depth anomalies, for the Ex 1997–1998 event. (b) Averaged C_p [ms^{-1}] for all El Niño events (1997–1998, 2002–2003, 2008–2009, 2012–2013, 2014, 2015–2016, 2017, where Niño 1 + 2 >+ 0.5 anomaly)

of 50–56 days and the second highest peak to 30–32 days. The time lags for these two peaks were estimated as 1–5 days and 11–12 days respectively, that correspond to mean phase speeds at 1.85 and 0.53 ms^{-1}, respectively. Averaging phase speeds for those exceeds a coherence squire value 0.15, the mean phase speed is obtained as 0.87 ms^{-1}, which is consistent with the phase speeds estimated with many different methods for reanalysis data.

5. Discussions

Using a 27-year high-resolution reanalysis dataset, we detected and tracked eddies, including Puddies, in the Peru-Chile eastern boundary upwelling system. Previous studies have emphasized the dominant subsurface anticyclonic eddies over cyclones in the subsurface layer. The aim of this study is to document the main characteristics of surface and subsurface eddies, analyse their spatial temporal variability, and identify a possible link to the ENSO variability.

Eddy detection and tracking analysis revealed that subsurface-intensified anticyclonic eddies (54%) are more prevalent than cyclones, and that the former increase during warmer conditions and extreme warming events such as El Niño. We found a higher number of subsurface-intensified anticyclonic eddies (Puddies) compared to subsurface-intensified cyclones during extreme El Niño events in 1997–1998 and 2015–2016, as well as in other moderately warm years (2008, 2012 and 2014).

In contrast to the findings of Combes et al. (2015), who reported an inverse relationship between the volume of subsurface eddies and the 250-day-lagged Niño 3. 4 index for the entire Peru-Chile EBUS, our results suggest that subsurface anticyclonic eddies -Puddies- increase during El Niño and warm events. This discrepancy may reflect regional differences within the EBUS. Our conclusion is supported by the increase in EKE in the subsurface layer within the first 100 km from the coast during warm events. Similarly, Conejero et al. (2020) reported enhanced surface EKE off Peru during El Niño

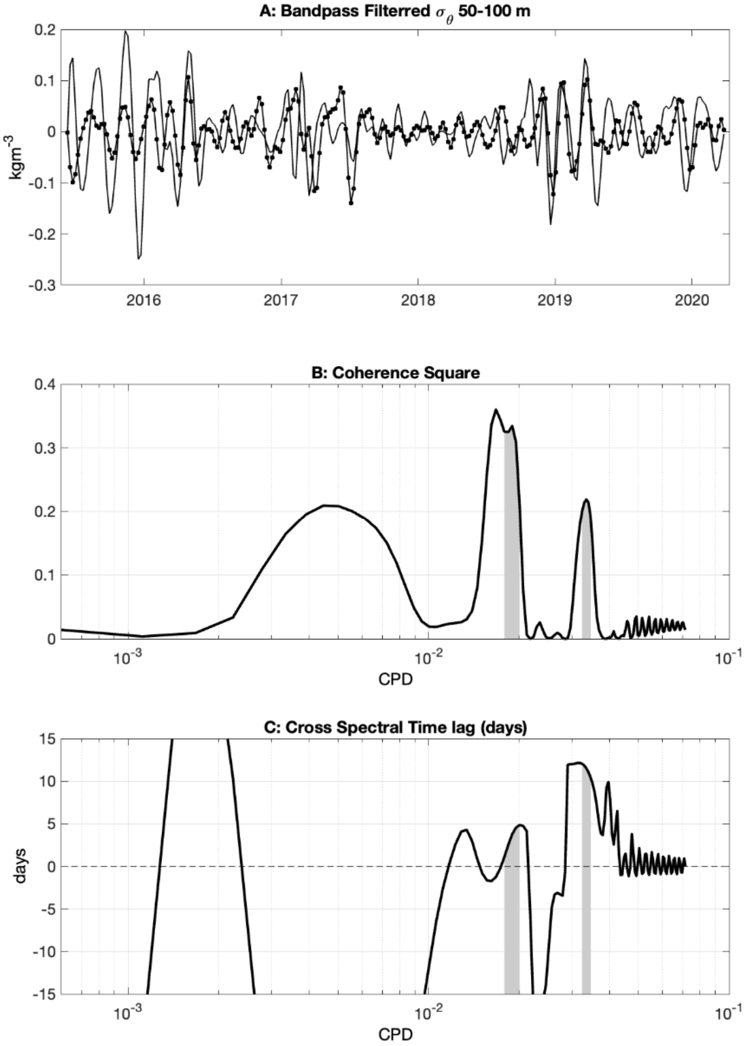

Fig. 13 Coherent analysis for observation at Chicama（7.8°S）and Callao（12°S）.（a）Time series of bandpass filtered（20–120 days）40–85 m-average σ_θ for（solid line）Chicama（7.8°S）and（dotted line）Callao（12°S）from 2015 through 2020.（b）Coherence square spectra of two time series shown in（a）.（c）Spectrum of the time lag（days）with positive values indicating Chicama leads Callao. Grey shaded regions indicate the frequency bands that exceed a coherence squire value 0.15 in（b）and（c）.

events. They also pointed out that EKE off Peru and Chile respond differently to El Niño, with EKE increasing off Peru and decreasing off Chile. This underscores the need to consider these regions separately when investigating ENSO-related variability. Hormazabal et al.（2004）, using in-situ mooring data off the Chilean coast（30°S）, found an inverse relationship between EKE and the Niño 3.4 index during 1997–1998, whereas Chaigneau et al. (2008) reported enhanced EKE off Peru during the same period, consistent with Conejero et al. (2020) and our results.

However, it should be noted that the increase in the number of tracked subsurface anticyclonic eddies is not proportional to the amplitude of warm events, although the warm events tend to be associated with relatively large numbers of subsurface anticyclonic eddies. For example, the most extreme warming during 1997–1998 did not yield the greatest number of subsurface anticyclonic eddies. This reflects on the positive but low correlation found between the number of subsurface eddies and the isopycnal depth. Instead, we found strong correspondences between the Niño index, EKE, and isopycnal depth variations. One possible explanation is that, in addition to the ENSO variability, local wind curl modulates the PCUC and the formation of Puddies. Another factor could be a limitation in the eddy detection and tracking, which may not perfectly capture all the eddies. Additionally, the decay of the coastal trapped Kelvin wave may differ from one event to another, which may vary the eddy dynamics in complex ways (Dewitte et al., 2012; Hormazabal et al., 2004; Czeschel et al., 2018).

Previous studies (Camayo and Campos, 2006; Belmadani et al., 2012) have shown that coastal trapped Kelvin waves in northern Peru propagate with periods of 80–120 days and that their periods can change as they interact with topographic features while traveling poleward. Some waves radiate Rossby waves, while others interact with the mesoscale eddies. Here, applying the coherence analysis for observation data from 2015 to 2020, we found that the subsurface density fluctuations with periods of 50–56 and 30–32 days translate poleward from Chicama through Callao with a speed C_p at 1.85 and 0.53 ms^{-1}, respectively. Averaging speeds for the data with coherence square higher than 0.15 and positive phases, the average phase speed is found to be 0.87 ms^{-1}. We also estimated C_p of the coastal trapped waves for the reanalysis data with a longer period (1993–2019) and higher spatial resolution. Using the cross-correlation analysis for isopycnal depth at σ_θ = 26 kgm^{-3} along 450 m isobath off Peru, the mean C_p is found to be 1.2 ms^{-1}, while C_p ranged from 0.5 ms^{-1} to 0.83 ms^{-1} with a poleward decreasing trend. These poleward phase speeds are in good agreement with the theoretical speeds for the first baroclinic mode internal Kelvin wave during El Niño events obtained by solving the vertical mode equation along 450 m isobath for their magnitude and a poleward decreasing trend (Camayo and Campos, 2006; Belmadani et al., 2012; Echevin et al., 2014).

Our analyses performed separately for surface and subsurface eddies, revealed distinct differences in their spatiotemporal distribution and associated characteristics. Surface eddies were found to be predominantly cyclonic (56%), with anticyclonic eddies accounting for the remaining 44%. Both types exhibited pronounced seasonal variability, with their highest occurrence from middle austral autumn, winter and early spring, and a marked decline later in the biggening of austral summer. On the other hand, subsurface anticyclones (54%) were found to dominate over cyclones (46%), with a marked seasonal pattern, peaking in abundance during the austral autumn (April) followed by austral winter season, and reaching their lowest numbers in the spring. The observed seasonality in surface eddy abundance is likely driven by intensified upwelling associated with seasonally varying winds patterns, while subsurface eddies appear to form primarily due to flow instabilities within the PCUC as it moves along the continental slope (Thomsen et al., 2016; Contreras et al., 2019).

Previous studies have demonstrated that surface eddies can be highly nonlinear, thus trapping and transporting water and its constituents. Our results indicate that surface cyclones tend to be more non-linear than anticyclones, consistent with earlier findings (e. g. Chelton et al. 2007; Nagai et al. 2015; Czeschel et al. 2018). Subsurface eddies also exhibit moderately strong non-linearity, suggesting that they can transport matter, albeit with somewhat leakier than surface eddies. On the other hand, subsurface anticyclones tend to live longer than their cyclonic counterparts or those at the surface. Given their longer lifetimes, subsurface anticyclones may exert a stronger influence on deeper layers. Most subsurface eddies have radii between 25 to 30 km, while about 66% of anticyclones have radii smaller than 35 km. Cyclones tend to be smaller, with 83% having radii less than 35 km.

Although our study marks a significant advance in understanding the characteristics of surface and subsurface eddies in the Peruvian EBUS region, we also acknowledge some limitations. We focused on data from the last 27 years and did not include earlier extreme events (e.g. Ex 1972–1973, Ex 1982–1983, EP 1986–1987, EP 1991–1992 events) that would have bolstered our conclusions. The eddy detection and tracking methods we used are not perfect to track the eddies from their generation to dissipation. The detection criterion based on the layer average parameters such as OW could become unsatisfied to determine it as an eddy, leading to interruption of the tracking. This would have introduced cases where Puddies formed away from the PCUC. In addition, the reanalysis data assimilate the observation data that most likely do not cover entire lifetime of each eddy. Thus, although reanalysis data are very useful to investigate the interannual variations of eddy field on average, it can be difficult to trace back the origin of each eddy by using the eddy detection and tracking techniques for the reanalysis data. The high-resolution numerical simulations covering equatorial and Eastern Pacific regions forced with realistic surface forcing are, therefore, ideal to achieve more accurate analyses especially on subsurface eddies and their interannual modulations.

Furthermore, we did not address the biological responses to mesoscale variability under ENSO and non-ENSO conditions. Future research should integrate longer datasets and high-resolution modelling for both physics and biogeochemistry to account for seasonal and interannual modulations of the PCUC. Such comprehensive approaches would provide a more holistic understanding of this complex upwelling system, which is strongly influenced by ENSO dynamics.

6. Conclusions

In this study, we investigated the spatial-temporal variability of surface and subsurface eddies in the Peruvian eastern boundary upwelling system (EBUS) by employing high-resolution reanalysis and observational data. The reanalysis data successfully reproduced the interannual variability observed in the region.

Although previous research has primarily focused on surface-intensified eddies, this work offers new insights into the less explored subsurface-intensified eddies. We characterized their fundamental properties, explored their temporal and spatial variability, and assessed their response to extreme climate events such as El Niño and La Niña. We summarize the results of the analyses as follows.

1. Prevalence and characteristics of subsurface eddies: subsurface anticyclones (Puddies) dominate the subsurface layer, accounting for ≈ 54% of all detected subsurface eddies. They show a pronounced seasonal cycle, with peak occurrences during austral autumn and early winter, corresponding to seasonal variability in eddy kinetic energy (EKE) and modulation of the Peru-Chile undercurrent (PCUC). Puddies are primarily concentrated in the central to southern regions of the study area. They tend to be highly nonlinear, exhibit larger radii (25–30 km) and possess longer lifetimes (up to 245 days) compared to their cyclonic counterparts.
2. Response to climatic extremes: Between 1993 and 2019, subsurface anticyclones (Puddies) exhibited significant variability in response to climate extremes. Their abundance was closely tied to periods of elevated EKE, particularly during El Niño events and moderately warm years. Conversely, their occurrence declined markedly during La Niña events, notably in 2007 and 2010.
3. Contrasting mechanisms for surface and subsurface eddies: Surface-intensified eddies are predominantly influenced by winds and surface currents, whereas subsurface eddies are more sensitive to changes in the PCUC and the thermocline structure, especially under ENSO conditions. During El Niño events, the arrival of the equatorial warm pool induces thermocline deepening and enhances the PCUC along the Peruvian slope. This deepening is associated with coastal trapped waves, which are generated following the arrival of equatorial Kelvin wave at the eastern boundary. Phase speeds derived from the vertical mode equation for the first baroclinic mode Kelvin wave along the 450-m isobath showed a range 0.8–1.7 ms^{-1} with a decreasing trend toward higher latitudes, consistent with the estimated phase speeds for the reanalysis data using the cross-correlations, C_p = 1.2 m s^{-1}, and 1st order polynomial fitting, C_p ranging between 0.5 m s^{-1} to 0.83 m s^{-1} during El Niño events. Furthermore, phase speed estimated from coherence analysis for the observational data indicated mean C_p = 0.87 ms^{-1} between Chicama (7.8°S) and Callao (12 °S), which is also in good agreement with that for the reanalysis data and the solution of the vertical mode equation.

These findings agree with prior studies and highlight a significant event-dependent variations between different El Niño types. Coastal trapped waves enhance subsurface eddy activity by modulating stratification and current strength, which might suggest that coastal trapped wave can act as critical intermediaries, linking large scale equatorial variability with local subsurface eddy dynamics in the Peruvian EBUS.

Acknowledgements. We are grateful to the Japanese Ministry of education, culture, sports, science and technology (MEXT) for the financial support provided during the doctoral course of GR. This research was funded by Japan Promotion of Science (JSPS), KAKENHI (23H04818, 23H01244, 24H02224) granted to TN. We thank the Peruvian Sea Institute (IMARPE) for providing in-situ observations used in this study, which are available by request.

References

Belmadani, A., Echevin, V., Dewitte, B., and Colas, F. (2012): Equatorially forced intraseasonal propagations along the Peru-Chile coast and their relation with the nearshore eddy activity in 1992–2000: A modeling study, Journal of Geophysical Research, 117, 4025, 360, https://doi.

org/10.1029/2011JC007848.

Bertrand, A., Lengaigne, M., Takahashi, K., Avadí, A., Florence, P., and Chris, H. (2020): El Niño Southern Oscillation (ENSO) effects on fisheries and aquaculture, FAO Fisheries and Aquaculture Technical Paper No. 660., Rome, ISBN 9789251323274,https://doi.org/10.4060/ca8348en.

Camayo, R. and Campos, E. J. (2006): Application of wavelet transform in the study of coastal trapped waves off the west coast of South America, Geophysical Research Letters, 33, 1–5, https://doi.org/10.1029/2006GL026395.

Chaigneau, A., Gizolme, A., and Grados, C. (2008): Mesoscale eddies off Peru in altimeter records: Identification algorithms and eddy spatio-temporal patterns, Progress in Oceanography, 79, 106–119, https://doi.org/10.1016/j.pocean.2008.10.013.

Chelton, D. B., Schlax, M. G., Samelson, R. M., and De Szoeke, R. A. (2007): Global observations of large oceanic eddies, Geophysical Research Letters, 34,https://doi.org/10.1029/2007GL030812.

Chelton, D. B., Schlax, M. G., and Samelson, R. M. (2011): Global observations of nonlinear mesoscale eddies, Progress in Oceanography, 91, 167–216, https://doi.org/10.1016/j.pocean.2011.01.002.

Colas, F., Mcwilliams, J. C., Capet, X., and Kurian, J. (2012): Heat balance and eddies in the Peru-Chile current system, Climate Dynamics, 39, 509–529, https://doi.org/10.1007/s00382-011-1170-6, 2012.

Combes, V., Hormazabal, S., and Lorenzo, E. D. (2015): Interannual variability of the subsurface eddy field in the Southeast Pacific, Journal of Geophysical Research: Oceans, 120, 4907–4924, https://doi.org/10.1002/2014JC010265.

Conejero, C., Dewitte, B., Garçon, V., Sudre, J., and Montes, I. (2020): ENSO diversity driving low-frequency change in mesoscale activity off Peru 375 and Chile, Scientific Reports, 10, https://doi.org/10.1038/s41598-020-74762-x.

Contreras, M., Pizarro, O., Dewitte, B., Sepulveda, H. H., and Renault, L. (2019): Subsurface mesoscale eddy generation in the ocean off central Chile, Journal of Geophysical Research: Oceans, 124, 5700–5722, https://doi.org/10.1029/2018JC014723.

Czeschel, R., Schütte, F., Weller, R. A., and Stramma, L. (2018): Transport, properties, and life cycles of mesoscale eddies in the eastern tropical South Pacific, Ocean Science, 14, 731–750, https://doi.org/10.5194/os-14-731-2018.

Dewitte, B., Vazquez-Cuervo, J., Goubanova, K., Illig, S., Takahashi, K., Cambon, G., Purca, S., Correa, D., Gutierrez, D., Sifeddine, A., and Ortlieb, L. (2012): Change in El Niño flavours over 1958–2008: Implications for the long-term trend of the upwelling off Peru, Deep-Sea Research Part II: Topical Studies in Oceanography, 77–80, 143–156, https://doi.org/10.1016/j.dsr2.2012.04.011.

Echevin V., Albert A., Lévy M., Graco M., Aumont O., Piétri A., and Garric G. (2014): Intraseasonal variability of nearshore productivity in the Northern Humboldt Current System: The role of coastal trapped waves, Continental Shelf Research, 73, 14–30, https://doi.org/10.1016/j.csr.2013.11.015.

Espinoza-Morriberón, D., Echevin, V., Colas, F., Tam, J., Ledesma, J., Vásquez, L., and Graco, M. (2017): Impacts of El Niño events on the Peruvian upwelling system productivity, Journal of Geophysical Research: Oceans, 122, 5423–5444, https://doi.org/10.1002/2016JC012439.

Espinoza-Morriberón, D., Echevin, V., Colas, F., Tam, J., Gutierrez, D., Graco, M., Ledesma, J., and Quispe-Ccalluari, C. (2019): Oxygen variability during ENSO in the Tropical South Eastern Pacific, Frontiers in Marine Science, 5, 1–20, https://doi.org/10.3389/fmars.2018.00526.

Flierl, G. R. (1981): Particle motions in large-amplitude wave fields. Geophysical & Astrophysical Fluid Dynamics, 18 (1–2), 39–74. https://doi.org/10.1080/03091928108208773.

Flores, R., Espino, M., luque, G., and Quispe, J. (2013): Patrones de variabilidad ambiental en el mar peruano, Revista Peruana de Biologia, 20, 21–28, http://www.scielo.org.pe/scielo.php?script=sci_arttext&pid=S1727-99332013000100004&nrm=iso.

Gruber, N., Lachkar, Z., Frenzel, H., Marchesiello, P., Münnich, M., Mcwilliams, J. C., Nagai, T., and Plattner, G. K. (2011): Eddy-induced reduction of biological production in eastern boundary upwelling systems, Nature Geoscience, 4, 787–792, https://doi.org/10.1038/ngeo1273.

Hormazabal, S., Shaffer, G., and Leth, O. (2004): Coastal transition zone off Chile, Journal of Geophysical Research: Oceans, 109, https://doi.org/10.1029/2003JC001956.

Kao, H.-Y. and Yu, J.-Y. (2009): Contrasting Eastern-Pacific and Central-Pacific types of ENSO, Journal of Climate, 22, 615 - 632, https://doi.org/10.1175/2008JCLI2309.1.

Kessler, W. S., Mcphaden, M. J., and Weickmann, K. M. (1995): Forcing of intraseasonal Kelvin waves in the equatorial Pacific, Journal of Geophysical Research, 100, https://doi.org/10.1029/95JC00382.

Lellouche, J.-M., Greiner, E., LE Galloudec, O., Garric, G., Regnier, C., Drevillon, M., Benkiran, M., Testut, C.-E., Bourdalle-Badie, R., Gasparin, F., Hernandez, O., Levier, B., Drillet, Y., Remy, E., and LE Traon, P.-Y. (2018): Recent updates to the Copernicus Marine Service global ocean monitoring and forecasting real-time 1/12° high-resolution system, Ocean Science, 14, 1093–1126, https://doi.org/10.5194/os-14-1093-2018.

Lukas, R. and Firing, E.: (1984) The geostrophic balance of the Pacific Equatorial Undercurrent, Deep-Sea Research Part A, Oceanographic Research 405 Papers, 31, 61–66, https://doi.org/10.1016/0198-0149 (84) 90072-4.

Molemaker, M. J., Mcwilliams, J. C., and Dewar, W. K. (2015): Submesoscale instability and generation of mesoscale anticyclones near a separation of the California Undercurrent, Journal of Physical Oceanography, 45, 613–629, https://doi.org/10.1175/JPO-D-13-0225.1.

Montes, I., Colas, F., Capet, X., and Schneider, W. (2010): On the pathways of the equatorial subsurface currents in the eastern equatorial Pacific and their contributions to the Peru-Chile Undercurrent, Journal of Geophysical Research: Oceans, 115, 1–16, 410, https://doi.org/10.1029/2009JC005710.

NAGAI, T., Gruber, N., Frenzel, H., Lachkar, Z., Mcwilliams, J. C., and Plattner, G. K. (2015): Dominant role of eddies and filaments in the offshore transport of carbon and nutrients in the California Current System, Journal of Geophysical Research: Oceans, pp. 5318–5341, https://doi.org/10.1002/2015JC010889.

Okubo, A. (1970): Horizontal dispersion of floatable particles in the vicinity of velocity singularities such as convergences, Deep-Sea Research, 17, 454–454.

Poli, L., Artana, C., and Provost, C. (2022): Topographically Trapped waves around South America with periods between 40 and 130 days in a global ocean reanalysis, Journal of Geophysical Research: Oceans, 127, https: //doi. org/10.1029/2021JC018067.

Ramírez, I. J. and Briones, F. (2017): Understanding the El Niño Costero of 2017: The definition problem and challenges of climate torecasting and disaster responses, International Journal of Disaster Risk Science, 8, 489–492, https://doi.org/10.1007/s13753-017-0151-8.

Rosales Quintana, G. M., Marsh, R., and Icochea Salas, L. A. (2021): Interannual variability in contributions of the Equatorial Undercurrent (EUC) to Peruvian upwelling source water, Ocean Science, 17, 1385–1402, https://doi.org/10.5194/os-17-1385-2021.

Santoso, A., Mcphaden, M. J., and Cai, W. (2017): The defining characteristics of ENSO extremes and the strong 2015/2016 El Niño, Reviews of Geophysics, 55, 1079–1129, https://doi.org/10.1002/2017RG000560.

Su, J., Xiang, B., Wang, B., and Li, T. (2014): Abrupt termination of the 2012 Pacific warming and its implication on ENSO prediction, Geophysical Research Letters, 41, 9058–9064, https://doi.org/10.1002/2014GL062380.

Takahashi, K. and Dewitte, B. (2016): Strong and moderate nonlinear El Niño regimes, Climate Dynamics, 46, 1627–1645, https://doi.org/10.1007/s00382-015-2665-3.

Thomsen, S., Kanzow, T., Krahmann, G., Greatbatch, R. J., DENGLER, M., and Lavik, G. (2016):

The formation of a subsurface anticyclonic eddy in the Peru-Chile Undercurrent and its impact on the near-coastal salinity, oxygen, and nutrient distributions, Journal of Geophysical Research: Oceans, 121, 476–501, https://doi.org/10.1002/2015JC010878.

Toggweiler, J. R., Dixon, K., and Broecker, W. S. (1991): The Peru upwelling and the ventilation of the south Pacific thermocline, Journal of Geophysical Research, 96, 20467, https://doi.org/10.1029/91JC02063.

Toniazzo, T. (2010): Climate variability in the south-eastern tropical Pacific and its relation with ENSO: A GCM study, Climate Dynamics, 34, 435 1093–1114, https://doi.org/10.1007/s00382-009-0602-z.

Vergara, O., Dewitte, B., Montes, I., Garçon, V., Ramos, M., and Pizarro, O. (2016): Seasonal variability of the oxygen minimum zone off Peru in a high-resolution regional coupled model, Biogeosciences, 13, 4389–4410, https://doi.org/10.5194/bg-13-4389-2016.

Weiss, J. (1991): The dynamics of enstrophy transfer in two-dimensional hydrodynamics, Physica D: Nonlinear Phenomena, 48, 273–294, https://doi.org/10.1016/0167-2789 (91) 90088-Q.

Received: December 23, 2024
Accepted: July 11, 2025